

SCIENTIFIC REPORTS

OPEN

Band gap bowing in $\text{Ni}_x\text{Mg}_{1-x}\text{O}$

Christian A. Niedermeier¹, Mikael Rålander¹, Sneha Rhode¹, Vyacheslav Kachkanov^{2,†}, Bin Zou¹, Neil Alford¹ & Michelle A. Moram¹

Epitaxial transparent oxide $\text{Ni}_x\text{Mg}_{1-x}\text{O}$ ($0 \leq x \leq 1$) thin films were grown on MgO(100) substrates by pulsed laser deposition. High-resolution synchrotron X-ray diffraction and high-resolution transmission electron microscopy analysis indicate that the thin films are compositionally and structurally homogeneous, forming a completely miscible solid solution. Nevertheless, the composition dependence of the $\text{Ni}_x\text{Mg}_{1-x}\text{O}$ optical band gap shows a strong non-parabolic bowing with a discontinuity at dilute NiO concentrations of $x < 0.037$. Density functional calculations of the $\text{Ni}_x\text{Mg}_{1-x}\text{O}$ band structure and the density of states demonstrate that deep Ni 3d levels are introduced into the MgO band gap, which significantly reduce the fundamental gap as confirmed by optical absorption spectra. These states broaden into a Ni 3d-derived conduction band for $x > 0.074$ and account for the anomalously large band gap narrowing in the $\text{Ni}_x\text{Mg}_{1-x}\text{O}$ solid solution system.

Received: 11 February 2016

Accepted: 14 July 2016

Published: 09 August 2016

The wide-band gap semiconductor NiO (3.7 eV) is one of the few p-type transparent conductive oxides demonstrating good electrical properties for application in optoelectronic devices¹. Thus NiO is used as a transparent hole transport layer in oxide p-n heterojunction devices such as electrical current rectifiers^{2,3}, ultraviolet (UV) photodetectors^{4,5} and light-emitting diodes^{6,7}. The epitaxial growth of high-crystal quality NiO thin films is desired, since polycrystalline films exhibit inferior electrical transport properties and may lead to higher leakage currents in p-n heterojunction devices.

The epitaxial growth of NiO on MgO single crystal substrates offers a promising platform for the preparation of complete UV-transparent oxide devices. Both NiO and MgO crystallize in the cubic rock-salt structure and $\text{Ni}_x\text{Mg}_{1-x}\text{O}$ thin films over the entire composition range can be grown with high crystalline quality on MgO single crystals⁸, having a structural mismatch of only 0.8% at maximum⁹. As compared to many other semiconductor alloys, the $\text{Ni}_x\text{Mg}_{1-x}\text{O}$ system is unique in demonstrating a great flexibility for band gap tuning from 3.7 eV to 7.8 eV¹⁰ in the deep UV region without the drawbacks of a significant change in lattice parameter or a phase transition. Therefore, $\text{Ni}_x\text{Mg}_{1-x}\text{O}$ is increasingly receiving interest for application in deep UV photodetectors^{8,11–14}. To tune the photosensitivity of these devices, it is essential to understand the $\text{Ni}_x\text{Mg}_{1-x}\text{O}$ band gap evolution as a function of composition and to be able to accurately describe it using an analytical equation.

Experimentally it has been shown that the band gap dependence in most semiconductor alloys or solid solutions $\text{A}_x\text{B}_{1-x}\text{C}$ as a function of composition x follows the parabolic function¹⁵

$$E_g = xE_g^{\text{AC}} + (1-x)E_g^{\text{BC}} - bx(1-x) \quad (1)$$

where E_g^{AC} and E_g^{BC} are the band gaps of the pure compounds AC and BC, respectively, and b is the bowing parameter. Since the band gap of the semiconductor alloy is generally smaller than indicated by the linear interpolation between the band gaps of its pure end members, the bowing parameter b is a positive constant. It has been proposed that the band gap bowing results from the aperiodic variation of the crystal potential in substitutional alloys, arising from random variations in occupation of the metal sites in the alloy by elements A and B, and its magnitude is a symmetric function of composition proportional to $x(1-x)$ ¹⁶.

The $\text{Ni}_x\text{Mg}_{1-x}\text{O}$ band gap dependence has been determined by optical absorption spectra of epitaxial thin films on MgO substrates prepared by molecular beam epitaxy¹⁷, textured thin films on quartz substrates prepared by magnetron sputtering^{14,18} and sol-gel spin coated thin films on quartz substrates¹⁹. Despite the large 7.8 eV MgO band gap, it has been observed that the $\text{Ni}_x\text{Mg}_{1-x}\text{O}$ band gap increases only marginally to 4.8 eV, even at a small NiO fraction of only 8 at.%. A density functional theory (DFT) calculation of the $\text{Ni}_x\text{Mg}_{1-x}\text{O}$ band gap dependence on composition has investigated superstructures with NiO contents of 25, 50 and 75 at.%²⁰. However,

¹Department of Materials, Imperial College London, Exhibition Road, London, SW7 2AZ, UK. ²Diamond Light Source Ltd, Diamond House, Chilton, Didcot, Oxfordshire, OX11 0DE, UK. [†]Present address: Tokamak Energy Ltd, 120A Olympic Avenue, Milton Park, Oxfordshire OX14 4SA, UK. Correspondence and requests for materials should be addressed to C.A.N. (email: c.niedermeier13@imperial.ac.uk)

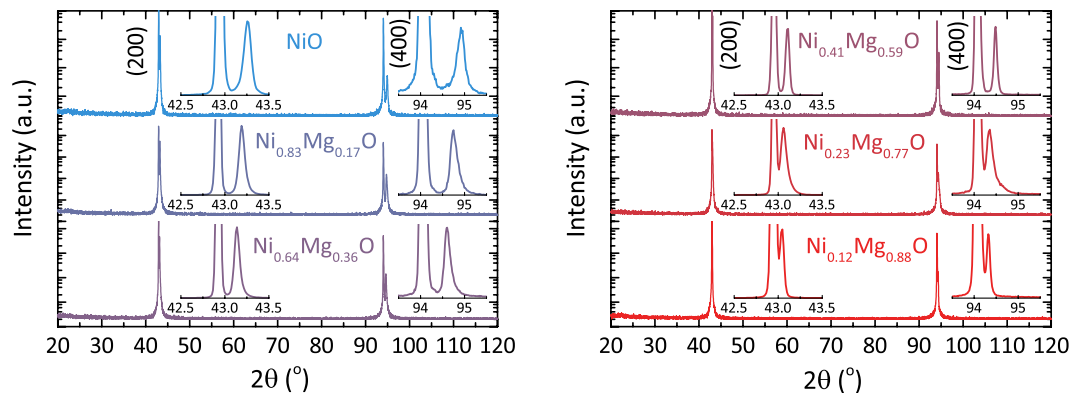


Figure 1. XRD $\omega - 2\theta$ patterns of $\text{Ni}_x\text{Mg}_{1-x}\text{O}$ thin films ($x = 1, 0.83, 0.64, 0.41, 0.23, 0.12$) prepared by pulsed laser deposition (PLD) showing the 100-oriented epitaxial growth on MgO(100) substrates. Insets show a magnification of the $\text{Ni}_x\text{Mg}_{1-x}\text{O}$ 200 and 400 diffraction peaks on a linear scale.

since the study excludes the dilute NiO concentration regime for $x < 0.25$, no band gap discontinuity has been identified and the underlying $\text{Ni}_x\text{Mg}_{1-x}\text{O}$ electronic band structure has not been investigated.

The present work combines experiment and theory to resolve the controversy over the $\text{Ni}_x\text{Mg}_{1-x}\text{O}$ band gap bowing. Regardless of the strongly non-parabolic band gap dependence on composition, the standard bowing theory has been rigidly applied in previous studies to describe the band gap evolution in the $\text{Ni}_x\text{Mg}_{1-x}\text{O}$ system^{11,12,14,18,20,21}. Through a detailed investigation of the $\text{Ni}_x\text{Mg}_{1-x}\text{O}$ microstructure and the underlying $\text{Ni}_x\text{Mg}_{1-x}\text{O}$ electronic structure with a particular focus on the dilute NiO concentration regime ($x = 0.125, 0.074$ and 0.037), the present work demonstrates that I) the origin of the irregular $\text{Ni}_x\text{Mg}_{1-x}\text{O}$ band gap dependence shall not be attributed to apparent structural or compositional inhomogeneities in $\text{Ni}_x\text{Mg}_{1-x}\text{O}$ films and II) the standard bowing theory is inapplicable to describe the non-parabolic composition dependence of the $\text{Ni}_x\text{Mg}_{1-x}\text{O}$ band gap because deep Ni 3d gap states evoke a highly anomalous bowing trend and significantly reduce the $\text{Ni}_x\text{Mg}_{1-x}\text{O}$ band gap even at small NiO fractions of only 3.7 at.%.

Results

Structural characterization of $\text{Ni}_x\text{Mg}_{1-x}\text{O}$ thin films. In the $\omega - 2\theta$ high resolution X-ray diffraction (HRXRD) patterns of the $\text{Ni}_x\text{Mg}_{1-x}\text{O}$ thin films ($x = 1, 0.83, 0.64, 0.41, 0.23, 0.12$) only the 200 and 400 diffraction peaks are observed, indicating that films are single-phase and grown in 100-orientation on the MgO(100) substrates (Fig. 1). Due to the marginal difference in lattice parameters between NiO (4.177 Å) and MgO (4.212 Å)⁹, the $\text{Ni}_x\text{Mg}_{1-x}\text{O}$ 200 and 400 diffraction peaks overlap with the corresponding peaks of the MgO substrate, especially for the $\text{Ni}_x\text{Mg}_{1-x}\text{O}$ specimens of high MgO content. The insets show a clear shift of the $\text{Ni}_x\text{Mg}_{1-x}\text{O}$ 200 and 400 diffraction peaks with increasing MgO fraction towards the MgO substrate peaks, indicating an increase in the out-of-plane lattice parameter.

The projection of the 3D reciprocal space maps of the $\text{Ni}_x\text{Mg}_{1-x}\text{O}$ 200 reflection along the reciprocal lattice vector Q_x recorded with 6 keV synchrotron radiation is given by an iso-intensity contour map on a logarithmic scale (Fig. 2). The increased X-ray wavelength of 2.067 Å as compared to the Cu $K_{\alpha 1}$ X-ray source of 1.5406 Å allows for a significantly improved spatial resolution of the high intensity 200 reflections of the $\text{Ni}_x\text{Mg}_{1-x}\text{O}$ thin film and MgO substrate. Note that the observation of multiple peaks for the MgO 200 substrate indicates the presence of additional macroscopic crystallographic domains (twins). The relatively narrow $\text{Ni}_x\text{Mg}_{1-x}\text{O}$ 200 diffraction peak in the in-plane Q_y direction in reciprocal space as compared to the MgO substrate indicates the high crystalline quality and low degree of mosaicity of the thin films. In particular, the out-of-plane width of the $\text{Ni}_x\text{Mg}_{1-x}\text{O}$ 200 diffraction peaks along Q_z ($x = 0.83, 0.64$ in Fig. 2(b,c)) does not indicate any compositional broadening as compared to the pure NiO thin film (Fig. 2(a)). The $\text{Ni}_x\text{Mg}_{1-x}\text{O}$ 200 diffraction peak shifts to smaller Q_z values with increasing MgO content in accordance with the slight increase in lattice parameter from NiO (4.177 Å) to MgO (4.212 Å). Reciprocal space map analysis of the asymmetric NiO 204 reflection shows that the in-plane lattice parameter a_x is larger than the unstrained reference (see Supplementary Fig. S1), indicating that the $\text{Ni}_x\text{Mg}_{1-x}\text{O}$ thin films are not completely relaxed, but strained to match the in-plane MgO substrate lattice parameter.

A cross-sectional scanning transmission electron microscopy high angle angular dark-field (STEM-HAADF) image of the $\text{Ni}_{0.23}\text{Mg}_{0.77}\text{O}$ film on MgO substrate acquired along the $\langle 001 \rangle$ zone axis is shown in Fig. 3(a). To locate the $\text{Ni}_{0.23}\text{Mg}_{0.77}\text{O}/\text{MgO}$ interface, a STEM energy dispersive X-ray spectroscopy (EDX) elemental map employing the Ni $L_{\alpha 3}$ (green) and Mg K_{α} (red) emission lines was recorded (Fig. 3(b)). The cross-sectional high resolution transmission electron microscopy (HRTEM) image of the $\text{Ni}_{0.23}\text{Mg}_{0.77}\text{O}/\text{MgO}$ interface acquired along the $\langle 001 \rangle$ zone axis using multi-beam conditions shows coherency and a defect-free $\text{Ni}_{0.23}\text{Mg}_{0.77}\text{O}$ bulk, demonstrating the single-domain epitaxy of the film on the MgO substrate (Fig. 3(c)). The very close lattice matching and coherent crystal interface between the $\text{Ni}_{0.23}\text{Mg}_{0.77}\text{O}$ film and MgO substrate is observed in the high magnification average background subtraction filtered (ABSF) HRTEM image (Fig. 3(d)) of the region indicated in Fig. 3(c).

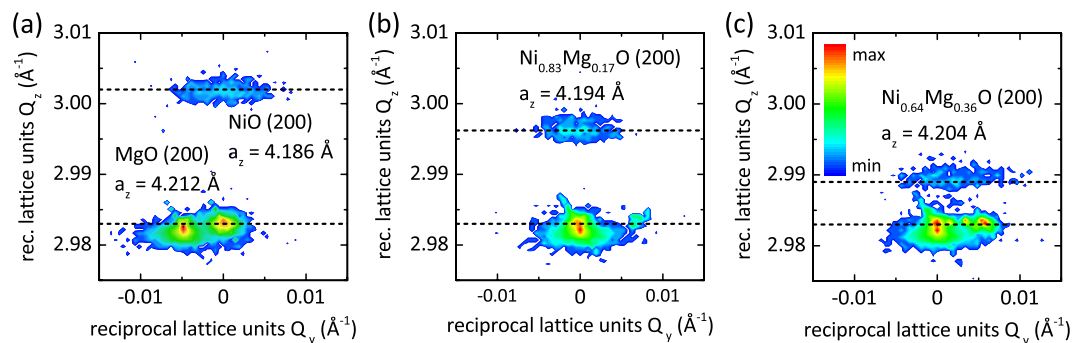


Figure 2. Projection of the 3D reciprocal space maps of the $\text{Ni}_x\text{Mg}_{1-x}\text{O}$ 200 reflection along the reciprocal lattice vector Q_x of $\text{Ni}_x\text{Mg}_{1-x}\text{O}$ thin films ($x = 1, 0.83, 0.64$) grown on $\text{MgO}(100)$ substrates recorded with 6 keV (2.067 Å) synchrotron radiation. The intensity of the diffraction peaks is given by an iso-intensity contour map on a logarithmic scale. The dashed lines give the local intensity maxima of the $\text{Ni}_x\text{Mg}_{1-x}\text{O}$ 200 and MgO 200 diffraction peaks as indicated.

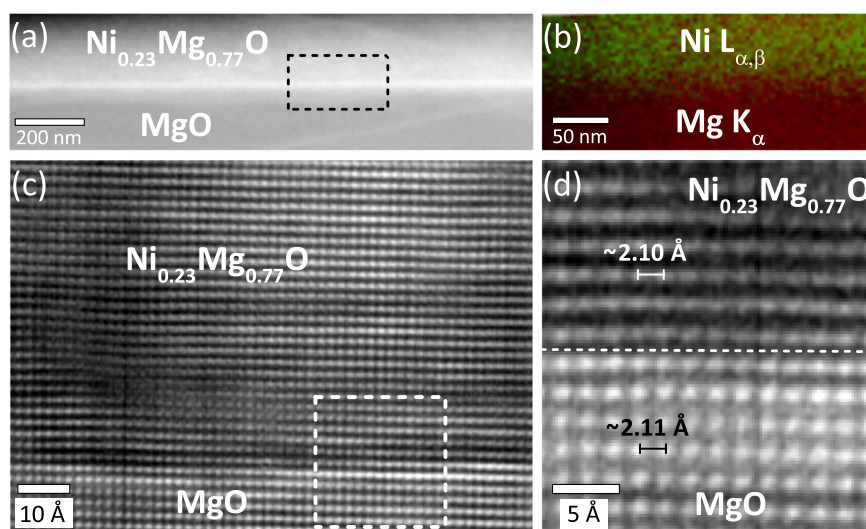


Figure 3. (a) Cross-sectional STEM-HAADF image of the $\text{Ni}_{0.23}\text{Mg}_{0.77}\text{O}/\text{MgO}$ interface acquired along the $\langle 001 \rangle$ zone axis and (b) STEM-EDX elemental map showing the $\text{Ni } L_{\alpha,\beta}$ (green) and $\text{Mg } K_{\alpha}$ (red) emission intensity for the area marked with the box in (a). (c) Cross-sectional HRTEM image of the $\text{Ni}_{0.23}\text{Mg}_{0.77}\text{O}/\text{MgO}$ interface acquired along the $\langle 001 \rangle$ zone axis demonstrating the single-domain epitaxial growth. (d) The high magnification ABSF HRTEM image of the region indicated with the box in (c) shows the coherent crystal interface between the $\text{Ni}_{0.23}\text{Mg}_{0.77}\text{O}$ thin film and the MgO substrate due to the nearly identical lattice spacing parameter d_{200} .

Optical transmission and band gap dependence. The optical transmission spectra of $\text{Ni}_x\text{Mg}_{1-x}\text{O}$ thin films ($x = 1, 0.83, 0.64, 0.41, 0.23, 0.17, 0.12$) indicate about 80% transparency in the visible and UV region until the onset of their fundamental absorption (Fig. 4(a)). The optical absorption blue-shifts with increasing MgO content in the $\text{Ni}_x\text{Mg}_{1-x}\text{O}$ thin films, from 340 nm for pure NiO to 200 nm for $\text{Ni}_{0.12}\text{Mg}_{0.88}\text{O}$. The calculated optical absorption spectra confirm the linear relationship between the photon energy $h\nu$ and $(\alpha h\nu)^2$, where α denotes the absorption coefficient, which is valid for direct transitions in semiconductors at the absorption edge (Fig. 4(b))²².

The composition dependence of the $\text{Ni}_x\text{Mg}_{1-x}\text{O}$ optical band gap as determined from the absorption spectra presented in this work is shown Fig. 5. The optical band gaps which have been determined in previous studies of $\text{Ni}_x\text{Mg}_{1-x}\text{O}$ thin films prepared by electron beam evaporation¹², molecular beam epitaxy¹⁷, magnetron sputtering^{14,18}, pulsed laser deposition²³ and sol-gel spin coating¹⁹ are included for comparison. In this work, the measured optical band gap of pure NiO is 3.7 eV and by alloying with MgO it increases linearly to 4.8 eV for $\text{Ni}_{0.12}\text{Mg}_{0.88}\text{O}$. Despite the small NiO fraction of only 12 at.%, it is striking to observe that the measured optical band gap remains 3 eV below that of pure MgO .

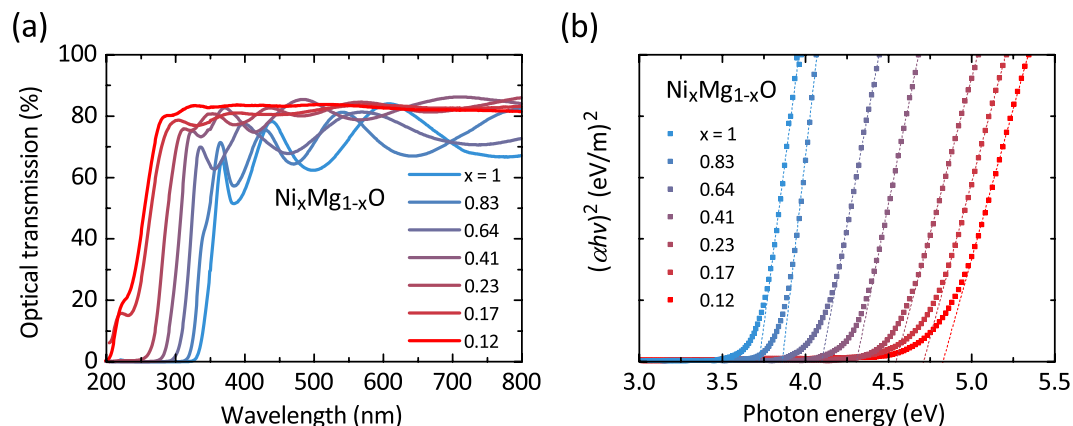


Figure 4. (a) Optical transmission of $\text{Ni}_x\text{Mg}_{1-x}\text{O}$ thin films ($x = 1, 0.83, 0.64, 0.41, 0.23, 0.17, 0.12$) in the UV-visible range from 200 nm to 800 nm. (b) Optical absorption showing the linear relationship between the photon energy $h\nu$ and $(\alpha h\nu)^2$, where α denotes the absorption coefficient, indicating a direct optical transition.

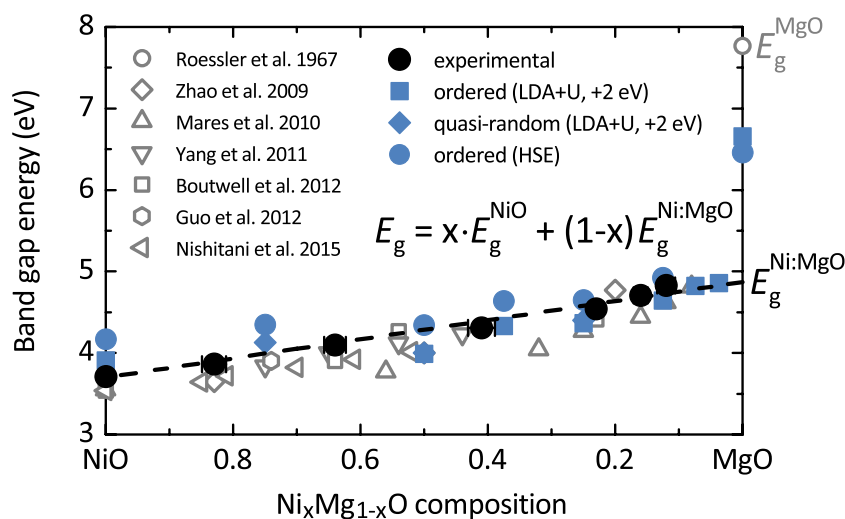


Figure 5. Experimental optical band gap of $\text{Ni}_x\text{Mg}_{1-x}\text{O}$ thin films ($x = 1, 0.83, 0.64, 0.41, 0.23, 0.17, 0.12$) obtained by absorption spectra (black filled circles). The error in the determination of the optical band gap is contained within the size of the data points. Calculated electronic band gaps of $\text{Ni}_x\text{Mg}_{1-x}\text{O}$ ($x = 1, 0.75, 0.5, 0.375, 0.25, 0.125, 0.074, 0.037, 0$) obtained from the DFT calculations of ordered (blue filled squares) and special quasi-random structures (blue filled diamonds), are shifted by +2 eV to account for the underestimation by the LDA + U method. In addition, the calculated electronic band gaps from the DFT calculation of ordered structures using the HSE approach are presented (blue filled circles). Experimental optical band gaps which have been determined by absorption and reflectance spectra in previous studies are included for comparison (grey empty symbols, after Roessler, D. M. *et al.*¹⁰, Zhao, Y. *et al.*¹², Nishitani, H. *et al.*¹⁴, Mares, J. W. *et al.*¹⁷, Yang, Z.-G. *et al.*¹⁸, Boutwell, R. *et al.*¹⁹ and Guo, Y. M. *et al.*²³).

Density functional theory calculation of the $\text{Ni}_x\text{Mg}_{1-x}\text{O}$ electronic structure. The calculated electronic band gaps obtained from DFT calculations of both ordered and special quasi-random structures (SQS) of $\text{Ni}_x\text{Mg}_{1-x}\text{O}$ are included in the band gap plot (Fig. 5). To account for the underestimation of the calculated band gaps for NiO (1.9 eV) and MgO (4.7 eV) applying the local density approximation (LDA + U) method, these values are shifted by +2 eV for comparison with experiment. The hybrid density functional calculations using the Heyd, Scuseria and Ernzerhof (HSE) approximation yields band gaps for NiO (4.2 eV) and MgO (6.5 eV) in good agreement with experiment. In consistency with the experimentally measured optical band gap trend, the calculations confirm that upon alloying with MgO, the $\text{Ni}_x\text{Mg}_{1-x}\text{O}$ band gap increases linearly over the entire investigated composition range ($1 \leq x \leq 0.037$). Both LDA + U and HSE calculation methods demonstrate that the variation in the band gap between NiO and $\text{Ni}_{0.125}\text{Mg}_{0.875}\text{O}$ is only about 0.7 eV. However, the difference between the calculated band gaps of $\text{Ni}_{0.037}\text{Mg}_{0.963}\text{O}$ and pure MgO of 1.8 eV is surprisingly large. More than 65% of the total band gap variation in the $\text{Ni}_x\text{Mg}_{1-x}\text{O}$ is observed after alloying just a few percent of NiO to MgO.

A superposition of the calculated band structure of $\text{Ni}_{0.074}\text{Mg}_{0.926}\text{O}$ and that of pure MgO obtained within the LDA + U method is shown in Fig. 6(a). It is striking to observe that the $\text{Ni}_{0.074}\text{Mg}_{0.926}\text{O}$ band structure shows deep

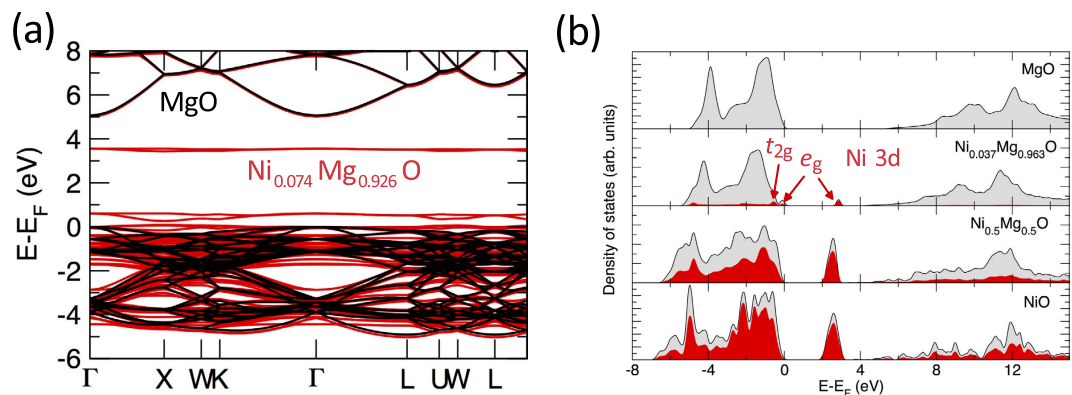


Figure 6. (a) Superposition of the electronic band structure of pure MgO (black) and $\text{Ni}_{0.074}\text{Mg}_{0.926}\text{O}$ (red) obtained within the LDA + U method showing deep localized states derived from Ni 3d e_g states inside the MgO band gap. The Fermi level E_F of MgO is located at the valence band maximum and the $\text{Ni}_{0.074}\text{Mg}_{0.926}\text{O}$ band structure is shifted to coincide with the MgO conduction band minimum. The $\text{Ni}_{0.074}\text{Mg}_{0.926}\text{O}$ states at the top of the valence band are all occupied. (b) Calculated DOS of $\text{Ni}_x\text{Mg}_{1-x}\text{O}$ ($x = 1, 0.5, 0.037$ and 0) indicating that the Ni 3d e_g states comprising the NiO conduction band remain as localized impurity states inside the MgO band gap for dilute NiO concentrations of 3.7 at.%. The partial DOS of Ni 3d states is shown in red.

localized levels almost entirely derived from Ni 3d e_g states at about 3 eV inside the MgO band gap. The Ni 3d e_g impurity-like level remains localized as there is only a negligible contribution from hybridization with O 2p states of the surrounding atoms. Both the $\text{Ni}_{0.074}\text{Mg}_{0.926}\text{O}$ valence and conduction band show a nearly unperturbed electronic structure derived from pure MgO. Since the extended states of the MgO conduction band are not affected by the localized Ni 3d e_g states, the approximation of employing a composition-independent +2 eV energy shift for the calculated band gaps obtained within the LDA + U method is justified to compare these results with experiment.

The calculated density of states (DOS) of $\text{Ni}_x\text{Mg}_{1-x}\text{O}$ ($x = 1, 0.5, 0.037$ and 0) is shown in Fig. 6(b). A small concentration of 3.7 at.% NiO in MgO creates localized states inside the MgO band gap: I) the energy level derived from Ni 3d e_g and t_{2g} states just above the MgO valence band, which is occupied, and II) the energy level almost entirely derived from Ni 3d e_g states at about 3.5 eV. Both of these features show localized levels similar to those introduced by impurities, even though a concentration of 3.7 at.% NiO is considered in the alloying regime. With increasing NiO concentration, the lower energy Ni 3d e_g and t_{2g} levels merge with the O 2p states at the top of the valence band while the density of the higher energy Ni 3d e_g impurity level increases and broadens to form the $\text{Ni}_{0.5}\text{Mg}_{0.5}\text{O}$ conduction band.

Discussion

By alloying with MgO, the NiO band gap increases about linearly from 3.7 eV to 4.9 eV in $\text{Ni}_{0.037}\text{Mg}_{0.963}\text{O}$. For MgO doped with impurity concentrations below 3.7 at.% NiO a band gap discontinuity is expected. It is obvious that the standard bowing equation cannot be applied to describe the anomalous $\text{Ni}_x\text{Mg}_{1-x}\text{O}$ band gap trend, because the bowing term $bx(1-x)$ only accounts for a parabolic deviation of the interpolated band gaps as a function of composition x , as a result of the aperiodic variation of the crystal potential in the random alloy.

The very narrow $\text{Ni}_x\text{Mg}_{1-x}\text{O}$ 200 diffraction spots obtained by HRXRD shown in Fig. 2 do not show any peak broadening in the out of plane Q_z component in reciprocal space indicating that compositional fluctuations on a macroscopic level are insignificant. Compositional inhomogeneities are further very unlikely to be observed as it has been shown experimentally that NiO and MgO are fully miscible, typically forming a homogeneous $\text{Ni}_x\text{Mg}_{1-x}\text{O}$ solid solution^{24,25}. A calorimetric investigation as well as thermodynamic modelling of the NiO-MgO system report a negative enthalpy of mixing describing a tendency towards atomic ordering rather than clustering^{26,27}. The microstructural homogeneity and high-quality epitaxial growth of the $\text{Ni}_x\text{Mg}_{1-x}\text{O}$ is evident from the HRTEM images showing a defect-free $\text{Ni}_x\text{Mg}_{1-x}\text{O}$ /MgO interface and suggesting single-domain epitaxial growth without evidence of either ordering or clustering (cf. Fig. 3).

The $\text{Ni}_x\text{Mg}_{1-x}\text{O}$ band gap bowing cannot be attributed to any transition in crystal structure, direct-to-indirect electronic transition or variation in compositional homogeneity. However, calculations of the electronic properties of semiconductor alloy systems have previously shown that the band gap bowing coefficient may nevertheless become largely composition dependent if the dilute alloy shows a localized deep impurity level in the band gap²⁸. When there is a pronounced difference in properties between the alloy end members, the impurities in the dilute alloy may create new electronic states rather than altering the host energy levels²⁹.

Electronic structure calculations of 3d transition metal (Fe, Co, Ni) impurities in MgO reveal that deep energy levels in the band gap are formed by combination of the metal 3d orbitals with O 2p orbitals to form e_g and t_{2g} states³⁰. Absorption spectra, cathodoluminescence and photoluminescence measurements of Ni-doped MgO crystals further indicate electronic transitions attributed to the energy levels of Ni^{2+} impurities³¹⁻³³. The DFT calculations presented in this work demonstrate that even at dilute NiO concentrations of 3.7 at.%, well beyond typical defect concentrations, there is only a small hybridization between the Ni 3d and MgO extended states, creating

such localized impurity-like levels inside the band gap. With increasing NiO content, the localized Ni 3d e_g states broaden to form the $\text{Ni}_x\text{Mg}_{1-x}\text{O}$ conduction band. The anomalous $\text{Ni}_x\text{Mg}_{1-x}\text{O}$ band gap narrowing is thus attributed to the fundamental difference in electronic structure between NiO and MgO, resulting in a remarkable modification of the MgO host band structure upon alloying with only a dilute amount of NiO ($x \leq 0.037$).

The origin of the $\text{Ni}_x\text{Mg}_{1-x}\text{O}$ band gap bowing is fundamentally different from that of most substitutional semiconductor alloys, for which the standard bowing equation holds. Instead, the non-parabolic $\text{Ni}_x\text{Mg}_{1-x}\text{O}$ bowing behaviour induced by the Ni 3d-derived localized states can be related to the band gap narrowing observed for highly mismatched III-V semiconductor alloys such as $\text{GaN}_x\text{As}_{1-x}$ ³⁴ and II-VI semiconductor alloys such as $\text{ZnS}_x\text{Te}_{1-x}$ ³⁵. Alloying of GaAs (ZnTe) with a small amount of N (S) introduces localized states at an energy level close to the conduction band edge, resulting in splitting of the conduction band into subbands and an effective narrowing of the fundamental gap^{36,37}. However, the $\text{Ni}_x\text{Mg}_{1-x}\text{O}$ solid solution system is different in that the localized Ni 3d e_g states remain as localized impurity states well inside the MgO band gap while no perturbation of the host conduction band structure is observed (cf. Fig. 6(a)). The $\text{Ni}_x\text{Mg}_{1-x}\text{O}$ solid solution presents a unique system in which cation substitution of a small percentage of Ni^{2+} for Mg^{2+} leads to a fundamental change in the electronic structure, while maintaining complete miscibility as well as structural stability over the entire composition range.

The $\text{Ni}_x\text{Mg}_{1-x}\text{O}$ band gap trend is best described by a linear interpolation of the NiO band gap E_g^{NiO} (3.7 eV) and that of MgO doped with an infinitesimal Ni impurity concentration $E_g^{\text{Ni:MgO}}$ (4.9 eV):

$$E_g(x) = xE_g^{\text{NiO}} + (1 - x)E_g^{\text{Ni:MgO}} \quad (2)$$

The results presented in this work show a critical concentration of about 7.4 at.% NiO in $\text{Ni}_x\text{Mg}_{1-x}\text{O}$ beyond which the defect-like impurity states become delocalized through the interaction of neighbouring Ni^{2+} cations distributed on the cation sublattice of the cubic rock-salt structure. For a random distribution of Ni^{2+} and Mg^{2+} cations on the face-centered cubic sublattice of $\text{Ni}_x\text{Mg}_{1-x}\text{O}$, the calculated site percolation threshold of nearest-neighbour Ni^{2+} cations is 19.9 at.% NiO³⁸. The observed threshold at about 7.4 at.% NiO defines a “localized-to-delocalized” transition (cf. ref. 29) at which the $\text{Ni}_x\text{Mg}_{1-x}\text{O}$ electronic structure changes from the characteristics of a concentrated $\text{Ni}_x\text{Mg}_{1-x}\text{O}$ solid solution with interacting Ni^{2+} cations to that of a dilute Ni:MgO solid solution with isolated Ni^{2+} impurity centres creating localized states in the MgO band gap. This indicates that the length scale over which Ni^{2+} - Ni^{2+} interactions can appear is greater than predicted assuming only nearest-neighbour interactions, or the non-random ordering of Ni^{2+} atoms on the cation sublattice sites decreases the probability of Ni^{2+} nearest-neighbour site occupation.

Conclusion

Despite forming a completely miscible and compositionally homogeneous solid solution, alloys of NiO and MgO exhibit a strikingly anomalous band gap bowing behaviour. The non-parabolic $\text{Ni}_x\text{Mg}_{1-x}\text{O}$ band gap dependence is attributed to the fundamental difference in electronic structure between NiO and MgO, resulting in a remarkable modification of the MgO host band structure upon alloying with only a dilute amount of NiO ($x \leq 0.037$). DFT calculations of the $\text{Ni}_x\text{Mg}_{1-x}\text{O}$ band structure and density of states demonstrate that localized Ni 3d impurity levels are introduced at an energy well below the MgO conduction band and account for the pronounced band gap narrowing as confirmed by optical absorption spectra. The standard bowing theory is inapplicable to describe the $\text{Ni}_x\text{Mg}_{1-x}\text{O}$ band gap dependence and may in general not be applied to semiconductor systems, for which one of the alloy end members creates such deep levels in the band gap.

Methods

Single-phase polycrystalline $\text{Ni}_x\text{Mg}_{1-x}\text{O}$ ceramic targets were prepared by sintering high purity NiO (99.999%) and MgO (99.995%) powders at temperatures of 1200–1550 °C for 5 h, applying higher temperatures for the targets of high MgO content. $\text{Ni}_x\text{Mg}_{1-x}\text{O}$ thin films were grown on single-crystal MgO (100) substrates by pulsed laser ablation of the $\text{Ni}_x\text{Mg}_{1-x}\text{O}$ ceramic targets using a 248 nm KrF excimer laser. The growth temperature was 600 °C and the deposition pressure was 0.7 Pa O_2 . The $\text{Ni}_x\text{Mg}_{1-x}\text{O}$ ceramic targets were ablated with a laser beam fluency of 0.8 J/cm² per pulse at a frequency of 10 Hz, resulting in a film thickness of about 300 nm.

The composition of the $\text{Ni}_x\text{Mg}_{1-x}\text{O}$ thin films was accurately determined by EDX in a JEOL JSM-6010LA scanning electron microscope (SEM). Using a primary beam voltage of 5 kV, EDX spectra of the Ni L_{α} (852 eV), Ni L_{β} (869 eV) and Mg K_{α} (1254 eV) X-ray emission lines were recorded. The background-corrected, integrated peaks of the Ni L_{α} , Ni L_{β} and the Mg K_{α} emission for all $\text{Ni}_x\text{Mg}_{1-x}\text{O}$ thin films were evaluated based on a calibration curve obtained using data from the polycrystalline $\text{Ni}_x\text{Mg}_{1-x}\text{O}$ targets of known composition. It was confirmed that the 5 kV primary electron beam is entirely probing the $\text{Ni}_x\text{Mg}_{1-x}\text{O}$ thin films and does not reach the MgO substrate by investigating $\text{Ni}_x\text{Mg}_{1-x}\text{O}$ thin films of equal layer thickness grown onto Si substrates for which the Si K_{α} emission (1740 eV) was not observed.

The crystal structure of the $\text{Ni}_x\text{Mg}_{1-x}\text{O}$ thin films on MgO substrates was studied by HRXRD employing a Philips PANalytical MRD diffractometer equipped with a Cu- $K_{\alpha 1}$ X-ray source (1.5406 Å) utilizing parallel beam geometry. The structure and crystalline quality of the $\text{Ni}_x\text{Mg}_{1-x}\text{O}$ thin films on MgO were further investigated by HRXRD carried out on beamline B16 at the Diamond Light Source, UK, using a 6 keV (2.067 Å) monochromated X-ray source. The area detector was fixed at the expected 2θ value of the $\text{Ni}_x\text{Mg}_{1-x}\text{O}$ 200 diffraction peak while scanning the incidence angle ω to record 2-dimensional δ - χ diffraction patterns, where δ is the angle between the detector arm and the horizontal plane and χ is the angle between the detector arm and the vertical plane. 3-dimensional (3D) reciprocal space maps were calculated from the obtained data set which show the $\text{Ni}_x\text{Mg}_{1-x}\text{O}$ 200 diffraction peak intensity as a function of the components of the scattering vector Q_x , Q_y and Q_z .

in reciprocal space. In this notation, Q_x and Q_y represent two orthogonal in-plane components and Q_z represents the out-of-plane component of the scattering vector in the specimen frame of reference.

The electron transparent cross-sectional TEM specimen was prepared by grinding, polishing and dimpling until the specimen thickness was below 10 μm , followed by Ar ion milling using a PIPS Ion miller (Gatan USA). Conventional HRTEM and STEM using the HAADF detector and STEM-EDX was performed using a JEOL 2100 microscope equipped with a field emission gun operating at 200 keV. The high magnification HRTEM image was filtered using an ABSF. STEM-HAADF and STEM-EDX studies were used to identify the $\text{Ni}_x\text{Mg}_{1-x}\text{O}/\text{MgO}$ interface. EDX spectral images were acquired recording Ni L_{α} , Ni L_{β} and Mg K_{α} X-ray emission lines and were analysed using the INCA software (ETAS group). The optical transmission of the $\text{Ni}_x\text{Mg}_{1-x}\text{O}$ thin films were measured with a Cary 5000 UV-Vis-NIR spectrophotometer using a bare MgO substrate as 100% transmission reference.

To describe the $\text{Ni}_x\text{Mg}_{1-x}\text{O}$ band gap trend, DFT calculations were performed using the LDA + U approach of Dudarev *et al.*³⁹ and the hybrid density functional HSE approximation^{40,41}. The LDA + U method was chosen in order to accurately describe the Ni 3d states because it significantly improves the performance of DFT applied to systems containing localised d electrons. The projector augmented wave method⁴² as implemented in the Vienna ab initio simulation package (VASP) was applied^{43,44}. A plane wave energy cut-off of 800 eV was used in the calculations and the minimum k-point density is 0.4 \AA^{-1} . For all $\text{Ni}_x\text{Mg}_{1-x}\text{O}$ calculations, the Coulomb and exchange energy parameters, $U = 4.3$ eV and $J = 1.0$ eV, were applied to the Ni 3d states according to previous studies⁴⁵. It is noted that the Dudarev approach to LDA + U only depends on an effective energy parameter $U_{\text{eff}} = U - J$ of 3.3 eV. The HSE approximation was chosen since it provides more accurate band gap values for semiconductors and insulators compared to traditional density functional approximations. In the HSE approximation the usual Hartree-Fock exchange mixing coefficient of 0.25 was used and the range separation parameter was set to 0.2 \AA^{-1} .

NiO is an antiferromagnet (AF), in which different Ni layers along the [111] direction have magnetic moments pointing in opposite directions. Thus magnetic moments on the Ni atoms in $\text{Ni}_x\text{Mg}_{1-x}\text{O}$ may order antiferromagnetically and therefore calculations on $\text{Ni}_x\text{Mg}_{1-x}\text{O}$ were performed based on the rock-salt derived structure of NiO with AF ordered layers of Ni atoms along the [111] direction (cf. refs 20 and 46). In the case of $\text{Ni}_{0.074}\text{Mg}_{0.926}\text{O}$, a $3 \times 3 \times 3$ repetition of the primitive rock-salt structure was used in which two Ni atoms substitute for two Mg atoms, while maintaining the AF coupling of the Ni moments. To describe the unordered $\text{Ni}_x\text{Mg}_{1-x}\text{O}$ solid solution, special quasi-random structures (SQS) were used^{47,48} and set up using the Alloy Theoretical Automated Toolkit (ATAT)⁴⁹ for $x = 0.75, 0.5$ and 0.25 . For all concentrations, the pair correlation functions for the first four atomic shells matched exactly with the pair correlation functions of the ideal unordered $\text{Ni}_x\text{Mg}_{1-x}\text{O}$ solid solution. Using this method the obtained structures contained a total of 64, 32 and 64 atoms for $x = 0.75, 0.5$ and 0.25 , respectively. In addition to the SQS model structures, calculations were performed using ordered supercells based on $2 \times 2 \times 2$ and $3 \times 3 \times 3$ repetitions of the rock-salt derived AF NiO structure. Both approaches were applied to investigate the influence of atomic ordering on the calculation results. The lattice constants of the $\text{Ni}_x\text{Mg}_{1-x}\text{O}$ solid solution were determined from the experimentally measured lattice constants of NiO (4.177 \AA) and MgO (4.212 \AA) according to Vegard's law⁹.

It shall be noted that other approaches such as the Green's function based methods employing the coherent potential approximation (CPA) can provide an accurate description of random compound alloys⁵⁰. The CPA is an effective method in describing the band structures of III-V alloys when disorder determines the band gap bowing^{51,52}, and in particular for calculation of detailed band properties such as effective masses and absorption line broadening⁵³. However, the single-site CPA does not account for local environment effects which can be important to describe semiconductors and require cluster expansion methods⁵⁴. The supercells used in this study are only idealized descriptions of the random system, since the structures are periodically repeated in space and therefore have a translational symmetry in contrast to the real random alloy. Therefore, certain effects found in real disordered systems, such as transition energy broadening due to disorder and corresponding lifetime effects are neglected in the supercell methods. Even so, for this study, SQS in combination with ordered supercells are employed which closely reproduce the physically most relevant correlation functions of the infinite, random alloy and thus provide an accurate description of the band gap bowing^{48,55}, while benefiting from a limited system size and reasonable computational effort.

References

1. Sato, H., Minami, T., Takata, S. & Yamada, T. Transparent conducting p-type NiO thin-films prepared by magnetron sputtering. *Thin Solid Films* **236**, 27 (1993).
2. Wong, H. F., Wong, K. H. & Lau, C. H. Electrical and optical properties of $\text{Li}_x\text{Ni}_{1-x}\text{O}/\text{In}_x\text{Mg}_x\text{Zn}_{1-x}\text{O}$ heteroepitaxial junction grown on TiN buffered Si. *Physica status solidi (a)* **206**, 2202 (2009).
3. Huang, C.-C., Wang, F.-H., Wu, C.-C., Huang, H.-H. & Yang, C.-F. Developing high-transmittance heterojunction diodes based on NiO/TZO bilayer thin films. *Nanoscale Research Letters* **8**, 206 (2013).
4. Ohta, H. Fabrication and photoresponse of a pn-heterojunction diode composed of transparent oxide semiconductors, p-NiO and n-ZnO. *Applied Physics Letters* **83**, 1029 (2003).
5. Long, H. *et al.* Photosensitive and temperature-dependent I-V characteristics of p-NiO film/n-ZnO nanorod array heterojunction diode. *Materials Science and Engineering: B* **184**, 44 (2014).
6. Wang, J.-Y. *et al.* Double side electroluminescence from p-NiO/n-ZnO nanowire heterojunctions. *Applied Physics Letters* **95**, 131117 (2009).
7. Jung, B. O., Kwon, Y. H., Seo, D. J., Lee, D. S. & Cho, H. K. Ultraviolet light emitting diode based on p-NiO/n-ZnO nanowire heterojunction. *Journal of Crystal Growth* **370**, 314 (2013).
8. Mares, J. W., Boutwell, R. C., Wei, M., Scheurer, A. & Schoenfeld, W. V. Deep-ultraviolet photodetectors from epitaxially grown $\text{Ni}_x\text{Mg}_{1-x}\text{O}$. *Applied Physics Letters* **97**, 161113 (2010).
9. Kuzmin, A. & Mironova, N. Composition dependence of the lattice parameter in $\text{Ni}_x\text{Mg}_{1-x}\text{O}$ solid solutions. *Journal of Physics: Condensed Matter* **10**, 7937 (1998).
10. Roessler, D. M. & Walker, W. C. Electronic Spectrum and Ultraviolet Optical Properties of Crystalline MgO. *Phys. Rev.* **159**, 733 (1967).

11. Ji, Z., He, Z., Liu, K., Zhao, S. & He, Z. Synthesis of $\text{Mg}_x\text{Ni}_{1-x}\text{O}$ thin films with a band-gap in the solar-blind region. *Journal of Crystal Growth* **273**, 446 (2005).
12. Zhao, Y. *et al.* MgNiO-based metal-semiconductor-metal ultraviolet photodetector. *Journal of physics D: Applied physics* **42**, 092007 (2009).
13. Guo, Y. *et al.* Enhanced performance of NiMgO-based ultraviolet photodetector by rapid thermal annealing. *Thin Solid Films* **558**, 311 (2014).
14. Nishitani, H. *et al.* Band gap tuning of $\text{Ni}_{1-x}\text{Mg}_x\text{O}$ films by radio-frequency sputter deposition for deep-ultraviolet photodetectors. *Applied Physics Express* **8**, 105801 (2015).
15. Thompson, A. G. & Woolley, J. C. Energy-Gap Variation in Mixed III-V Alloys. *Canadian Journal of Physics* **45**, 255 (1967).
16. Van Vechten, J. A. & Bergstresser, T. K. Electronic Structures of Semiconductor Alloys. *Phys. Rev. B* **1**, 3351 (1970).
17. Mares, J. W., Boutwell, R. C., Scheurer, A., Falanga, M. & Schoenfeld, W. V. Cubic $\text{Zn}_x\text{Mg}_{1-x}\text{O}$ and $\text{Ni}_x\text{Mg}_{1-x}\text{O}$ thin films grown by molecular beam epitaxy for deep-UV optoelectronic applications. *Proc. SPIE* **7603**, 76031B (2010).
18. Yang, Z.-G., Zhu, L.-P., Guo, Y.-M., Ye, Z.-Z. & Zhao, B.-H. Preparation and band-gap modulation in $\text{Mg}_x\text{Ni}_{1-x}\text{O}$ thin films as a function of Mg contents. *Thin Solid Films* **519**, 5174 (2011).
19. Boutwell, R., Wei, M., Scheurer, A., Mares, J. & Schoenfeld, W. Optical and structural properties of NiMgO thin films formed by sol-gel spin coating. *Thin Solid Films* **520**, 4302 (2012).
20. Deng, J., Mortazavi, M., Medhekar, N. V. & Zhe Liu, J. Band engineering of $\text{Ni}_{1-x}\text{Mg}_x\text{O}$ alloys for photocathodes of high efficiency dye-sensitized solar cells. *Journal of Applied Physics* **112**, 123703 (2012).
21. Kwon, Y. H., Chun, S. H. & Cho, H. K. Controllable band-gap engineering of the ternary $\text{Mg}_x\text{Ni}_{1-x}\text{O}$ thin films deposited by radio frequency magnetron sputtering for deep ultra-violet optical devices. *Thin Solid Films* **529**, 417 (2013).
22. Mott, N. F. & Davis, E. A. *Electronic Processes in Non-Crystalline Materials* (Oxford, Clarendon Press, 1971).
23. Guo, Y. M. *et al.* Valence band offset of n-ZnO/p-Mg $_x$ Ni $_{1-x}$ O heterojunction measured by x-ray photoelectron spectroscopy. *Applied Physical Letters* **101**, 052109 (2012).
24. Holgersson, S. & Karlsson, A. Röntgenographische Untersuchungen einiger Mischkristallsysteme mit Monoxyden als Komponenten. *Zeitschrift für anorganische und allgemeine Chemie* **182**, 255 (1929).
25. Wartenberg, H. V. & Prophet, E. Schmelzdiagramme höchstfeuerfester Oxyde. V. Systeme mit MgO. *Zeitschrift für anorganische und allgemeine Chemie* **208**, 369 (1932).
26. Davies, P. K. & Navrotsky, A. Thermodynamics of solid solution formation in NiO - MgO and NiO - ZnO. *Journal of Solid State Chemistry* **38**, 264 (1981).
27. Woo, D.-H., Lee, H.-G. & Jung, I.-H. Thermodynamic modeling of the NiO-SiO $_2$, MgO-NiO, CaO-NiO-SiO $_2$, MgO-NiO-SiO $_2$, CaO-MgO-NiO and CaO-MgO-NiO-SiO $_2$ systems. *Journal of the European Ceramic Society* **31**, 43 (2011).
28. Bellaiche, L., Wei, S.-H. & Zunger, A. Localization and percolation in semiconductor alloys: GaAsN vs GaAsP. *Phys. Rev. B* **54**, 17568 (1996).
29. Kent, P. R. C. & Zunger, A. Evolution of III-V Nitride Alloy Electronic Structure: The Localized to Delocalized Transition. *Phys. Rev. Lett.* **86**, 2613–2616 (2001).
30. Timmer, G. & Borstel, G. Electronic structure of nickel, iron, and cobalt impurities in magnesium oxide. *Phys. Rev. B* **43**, 5098 (1991).
31. Kroeger, F., Vink, H. & Boomgaard, J. V. D. Absorption and fluorescence of solid solutions MgO-NiO. *Physica* **18**, 77 (1952).
32. Pappalardo, R., Wood, D. L. & Linares, R. C. Optical Absorption Spectra of Ni-Doped Oxide Systems. I. *The Journal of Chemical Physics* **35**, 1460 (1961).
33. Duley, W. Multiphoton excitation of visible and VUV luminescence in MgO crystals. *Optics Communications* **51**, 160 (1984).
34. Weyers, M., Sato, M. & Ando, H. Red Shift of Photoluminescence and Absorption in Dilute GaAsN Alloy Layers. *Japanese Journal of Applied Physics* **31**, L853 (1992).
35. Seong, M. J., Alawadhi, H., Miotkowski, I., Ramdas, A. K. & Miotkowska, S. Oxygen isoelectronic impurity in $\text{ZnS}_x\text{Te}_{1-x}$. *Phys. Rev. B* **60**, R16275 (1999).
36. Shan, W. *et al.* Band Anticrossing in GaInNAs Alloys. *Phys. Rev. Lett.* **82**, 1221 (1999).
37. Walukiewicz, W. *et al.* Interaction of Localized Electronic States with the Conduction Band: Band Anticrossing in II-VI Semiconductor Ternaries. *Phys. Rev. Lett.* **85**, 1552 (2000).
38. Stauffer, D. & Aharony, A. *Introduction to Percolation Theory* (London: Taylor & Francis, 2nd edn 1992).
39. Dudarev, S. L., Botton, G. A., Savrasov, S. Y., Humphreys, C. J. & Sutton, A. P. Electron-energy-loss spectra and the structural stability of nickel oxide: An LSDA + U study. *Phys. Rev. B* **57**, 1505 (1998).
40. Heyd, J., Scuseria, G. E. & Ernzerhof, M. Hybrid functionals based on a screened Coulomb potential. *The Journal of Chemical Physics* **118**, 8207 (2003).
41. Heyd, J., Scuseria, G. E. & Ernzerhof, M. Erratum: 'Hybrid functionals based on a screened Coulomb potential' [J. Chem. Phys. 118, 8207 (2003)]. *The Journal of Chemical Physics* **124**, 219906 (2006).
42. Blöchl, P. E. Projector augmented-wave method. *Phys. Rev. B* **50**, 17953 (1994).
43. Kresse, G. & Furthmüller, J. Efficient iterative schemes for *ab initio* total-energy calculations using a plane-wave basis set. *Phys. Rev. B* **54**, 11169 (1996).
44. Kresse, G. & Joubert, D. From ultrasoft pseudopotentials to the projector augmented-wave method. *Phys. Rev. B* **59**, 1758 (1999).
45. Lany, S., Osorio-Guillén, J. & Zunger, A. Origins of the doping asymmetry in oxides: Hole doping in NiO versus electron doping in ZnO. *Phys. Rev. B* **75**, 241203 (2007).
46. Rödl, C., Fuchs, F., Furthmüller, J. & Bechstedt, F. Quasiparticle band structures of the antiferromagnetic transition-metal oxides MnO, FeO, CoO, and NiO. *Phys. Rev. B* **79**, 235114 (2009).
47. Zunger, A., Wei, S.-H., Ferreira, L. G. & Bernard, J. E. Special quasirandom structures. *Phys. Rev. Lett.* **65**, 353 (1990).
48. Wei, S.-H., Ferreira, L. G., Bernard, J. E. & Zunger, A. Electronic properties of random alloys: Special quasirandom structures. *Phys. Rev. B* **42**, 9622 (1990).
49. van de Walle, A. *et al.* Efficient stochastic generation of special quasirandom structures. *Calphad* **42**, 13 (2013).
50. Ruban, A. V. & Abrikosov, I. A. Configurational thermodynamics of alloys from first principles: effective cluster interactions. *Reports on Progress in Physics* **71**, 046501 (2008).
51. Chen, A.-B. & Sher, A. Gap Variation in Semiconductor Alloys and the Coherent-Potential Approximation. *Phys. Rev. Lett.* **40**, 900 (1978).
52. Chen, A.-B. & Sher, A. Electronic structure of pseudobinary semiconductor alloys $\text{Al}_x\text{Ga}_{1-x}\text{As}$, $\text{GaP}_x\text{As}_{1-x}$, and $\text{Ga}_x\text{In}_{1-x}\text{P}$. *Phys. Rev. B* **23**, 5360 (1981).
53. Chen, A.-B. & Sher, A. Valence-band structures of III-V compounds and alloys - Bond-orbital and coherent-potential approximations. *Phys. Rev. B* **17**, 4726 (1978).
54. Gonis, A. & Garland, J. W. Multishell method: Exact treatment of a cluster in an effective medium. *Phys. Rev. B* **16**, 2424 (1977).
55. Bellaiche, L., Wei, S.-H. & Zunger, A. Band gaps of GaPN and GaAsN alloys. *Applied Physics Letters* **70**, 3558 (1997).

Acknowledgements

We acknowledge support from the Leverhulme Trust via M.A. Moram's Research Leadership Award (RL-0072012) and from Diamond Light Source via proposal MT9149. M.A. Moram acknowledges further support from the Royal Society through a University Research Fellowship. We acknowledge use of the Imperial College high performance computing service, via our membership of the UK's HEC Materials Chemistry Consortium funded by EPSRC (EP/L000202), and use of the ARCHER UK national supercomputing service (<http://www.archer.ac.uk>).

Author Contributions

C.A.N. conceived and performed the experiments and prepared the manuscript. M.R. performed the theoretical calculations and prepared the DFT section of the manuscript. S.R. obtained the TEM micrographs and V.K. provided assistance with synchrotron HRXRD measurements. C.A.N., M.R., B.Z., N.A. and M.A.M. discussed the results. All authors reviewed the manuscript.

Additional Information

Supplementary information accompanies this paper at <http://www.nature.com/srep>

Competing financial interests: The authors declare no competing financial interests.

How to cite this article: Niedermeier, C. A. *et al.* Band gap bowing in $\text{Ni}_x\text{Mg}_{1-x}\text{O}$. *Sci. Rep.* **6**, 31230; doi: 10.1038/srep31230 (2016).



This work is licensed under a Creative Commons Attribution 4.0 International License. The images or other third party material in this article are included in the article's Creative Commons license, unless indicated otherwise in the credit line; if the material is not included under the Creative Commons license, users will need to obtain permission from the license holder to reproduce the material. To view a copy of this license, visit <http://creativecommons.org/licenses/by/4.0/>

© The Author(s) 2016